

Supporting Information for

**Unravelling Phase-Dependent Electronic Dimensionality and
Optoelectronic Properties in Lead-Free $A_3B_2X_9$ Perovskites for
Photovoltaic Applications**

Qingyuan Luo¹, Dabao Xie¹, Yiqian Tian¹, Congmin Zhang¹, Dan Cao², Xiaoshuang
Chen³, Pei Liang¹ and Haibo Shu^{1,*}

¹College of Optical and Electronic Technology, China Jiliang University, Hangzhou
310018, China.

²College of Science, China Jiliang University, Hangzhou 310018, China

³State Key Laboratory of Infrared Physics, Shanghai Institute of Technical Physics,
Chinese Academy of Science, Shanghai 200083, China

*Corresponding author. Email: shuhaibo@cjlu.edu.cn

CONTENTS

- S1. The SOC effect on the band structure of $A_3B_2X_9$ perovskites
- S2. Effect of materials thickness on the PCE of $A_3B_2X_9$ perovskites
- S3. Synthetic conditions and phase structures of $A_3B_2X_9$ perovskites in experiment
- S4. Projected band structures of $A_3B_2X_9$ perovskites in H and T phases
- S5. Projected density of states of $Cs_3Sb_2I_9$ perovskite in H and T phases
- S6. Illustration of the band-edge orbital coupling in $A_3B_2X_9$ perovskites
- S7. The comparison between the calculated and experimental bandgaps of some $A_3B_2X_9$ perovskites
- S8. Optical absorption spectra of $A_3B_2X_9$ perovskites in H and T phases
- S9. The computational details for intrinsic defects of T-phase $Cs_3Sb_2I_9$
- S10. Thickness effect on electronic structures of 2D T-phase $Cs_3B_2X_9$ nanosheets
- S11. Thickness effect on optical absorption of 2D T-phase $Cs_3B_2X_9$ nanosheets

S1. The SOC effect on the band structure of $A_3B_2X_9$ perovskites

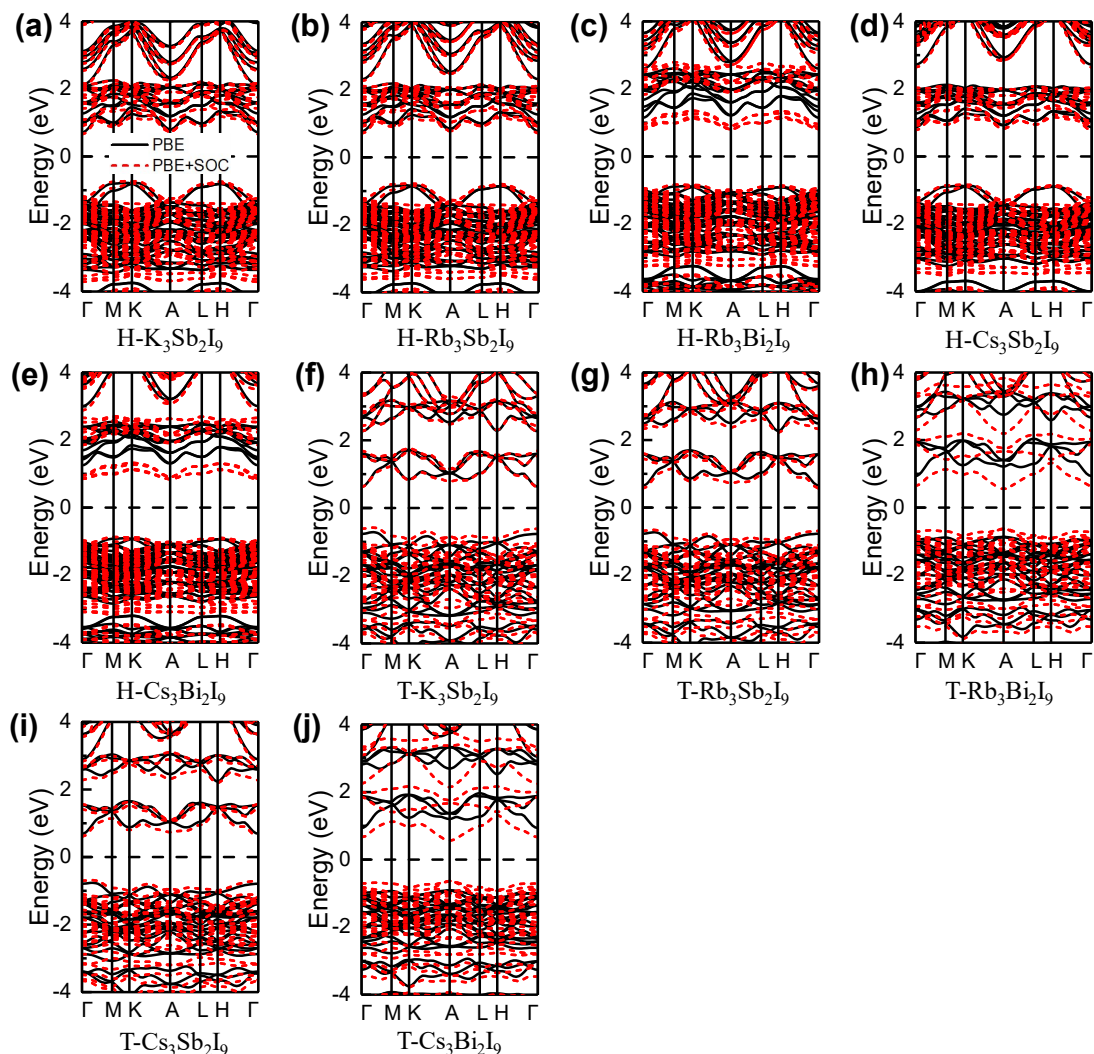


Fig. S1 Band structures of $A_3B_2I_9$ perovskites calculated by the PBE functional with and without SOC. The band structure of (a) H-phase $K_3Sb_2I_9$, (b) H-phase $Rb_3Sb_2I_9$, (c) H-phase $Rb_3Bi_2I_9$, (d) H-phase $Cs_3Sb_2I_9$, (e) H-phase $Cs_3Bi_2I_9$, (f) T-phase $K_3Sb_2I_9$, (g) T-phase $Rb_3Sb_2I_9$, (h) T-phase $Rb_3Bi_2I_9$, (i) T-phase $Cs_3Sb_2I_9$, and (j) T-phase $Cs_3Bi_2I_9$. The dash lines and solid lines denote the band structures calculated with and without the SOC effect, respectively. The horizontal dash lines at the energy zero point denote the position of Fermi level.

Using ten $A_3B_2I_9$ perovskite structures as examples, their band structures are calculated by the PBE functional with and without SOC effect (Fig. S1). The band structures of $A_3B_2I_9$ perovskites calculated by the PBE+SOC notably deviate from those obtained by the PBE functional. More specifically, the SOC effect induces the downshift of bands at the lower conduction band and upshift of bands at the higher valence band, resulting in the reduction of bandgap in these perovskites. Therefore, the SOC effect has been considered in the calculations of this work.

S2. Effect of materials thickness on the PCE of $A_3B_2X_9$ perovskites

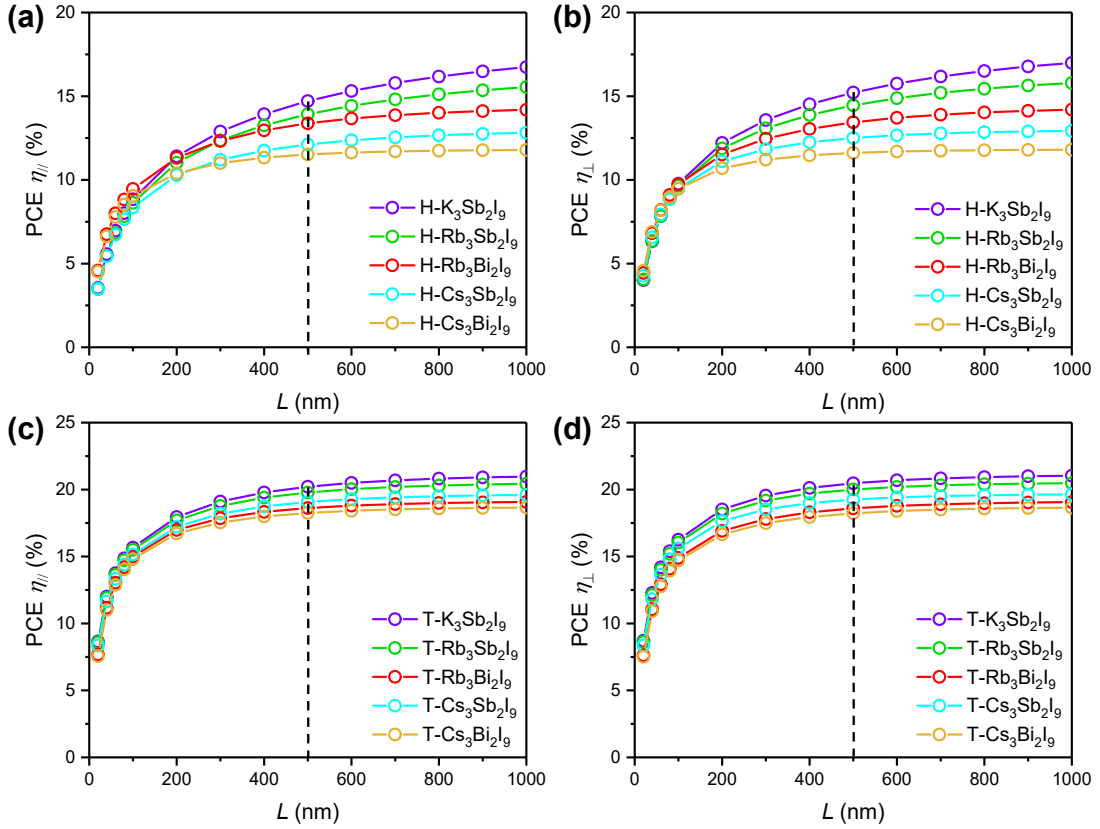


Fig. S2 PCE (η) of $A_3B_2X_9$ perovskites as a function of material thickness (L). (a,b) Thickness dependent PCE of H-phase $A_3B_2I_9$ perovskites along the (a) in-plane ($\eta_{||}$) and (b) out-of-plane (η_{\perp}) direction. (c,d) Thickness dependent PCE of T-phase $A_3B_2I_9$ perovskites along the (c) in-plane ($\eta_{||}$) and (d) out-of-plane (η_{\perp}) direction.

Using ten $A_3B_2I_9$ perovskite structures as examples, the material thickness effect on the PCE of these perovskites are predicted by equation (6) described in main text. As shown in Fig. S2, it can be seen that the PCE value of these perovskites indicates an increase trend with increasing thickness (L) of perovskite thin films and tends to be saturated when L arrives at ~ 500 nm. Therefore, the maximum PCE value of $A_3B_2I_9$ perovskites is predicted by using $L = 500$ nm.

S3. Synthetic conditions and phase structures of $A_3B_2X_9$ perovskites in experiment

Table S1 Synthetic conditions and phase structures of $A_3B_2X_9$ perovskites reported in experiment.

Materials	Phase	Temperature (K)	Precursors	Method	Ref.
$Cs_3Sb_2Cl_9$	T	313-358	CsCl+SbCl ₃	Solution method	[1]
$Cs_3Sb_2Br_9$	T	403	CsBr+SbBr ₃	Solution method	[2]
$Cs_3Sb_2I_9$	T	973	CsI+SbI ₃	CVD	[3]
$Cs_3Sb_2I_9$	H	348	CsI+SbI ₃	Solution method	[4]
$Cs_3Bi_2Cl_9$	T	433	Bi(OAc) ₃ +Cs ₂ CO ₃	Solution method	[5]
$Cs_3Bi_2Br_9$	T	353	CsBr+BiBr ₃	Solution method	[6]
$Cs_3Bi_2I_9$	H	973	CsI+BiI ₃	CVD	[3]

S4. Projected band structures of $A_3B_2X_9$ perovskites in H and T phases

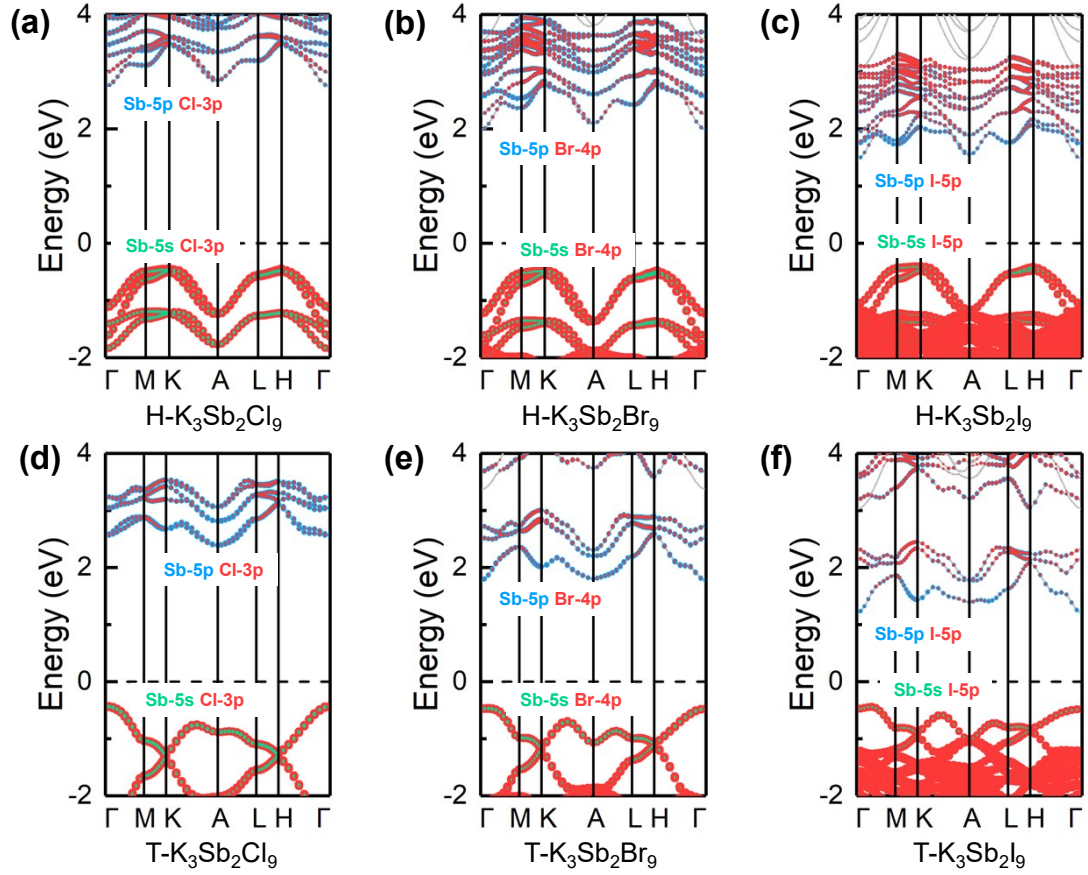


Fig. S3 Projected band structures of $K_3B_2X_9$ ($B = Sb$) perovskites in H and T phases. Projected band structure of (a) H-phase $K_3Sb_2Cl_9$, (b) H-phase $K_3Sb_2Br_9$, (c) H-phase $K_3Sb_2I_9$, (d) T-phase $K_3Sb_2Cl_9$, (e) T-phase $K_3Sb_2Br_9$, (f) T-phase $K_3Sb_2I_9$. The dash lines denote the position of Fermi level.

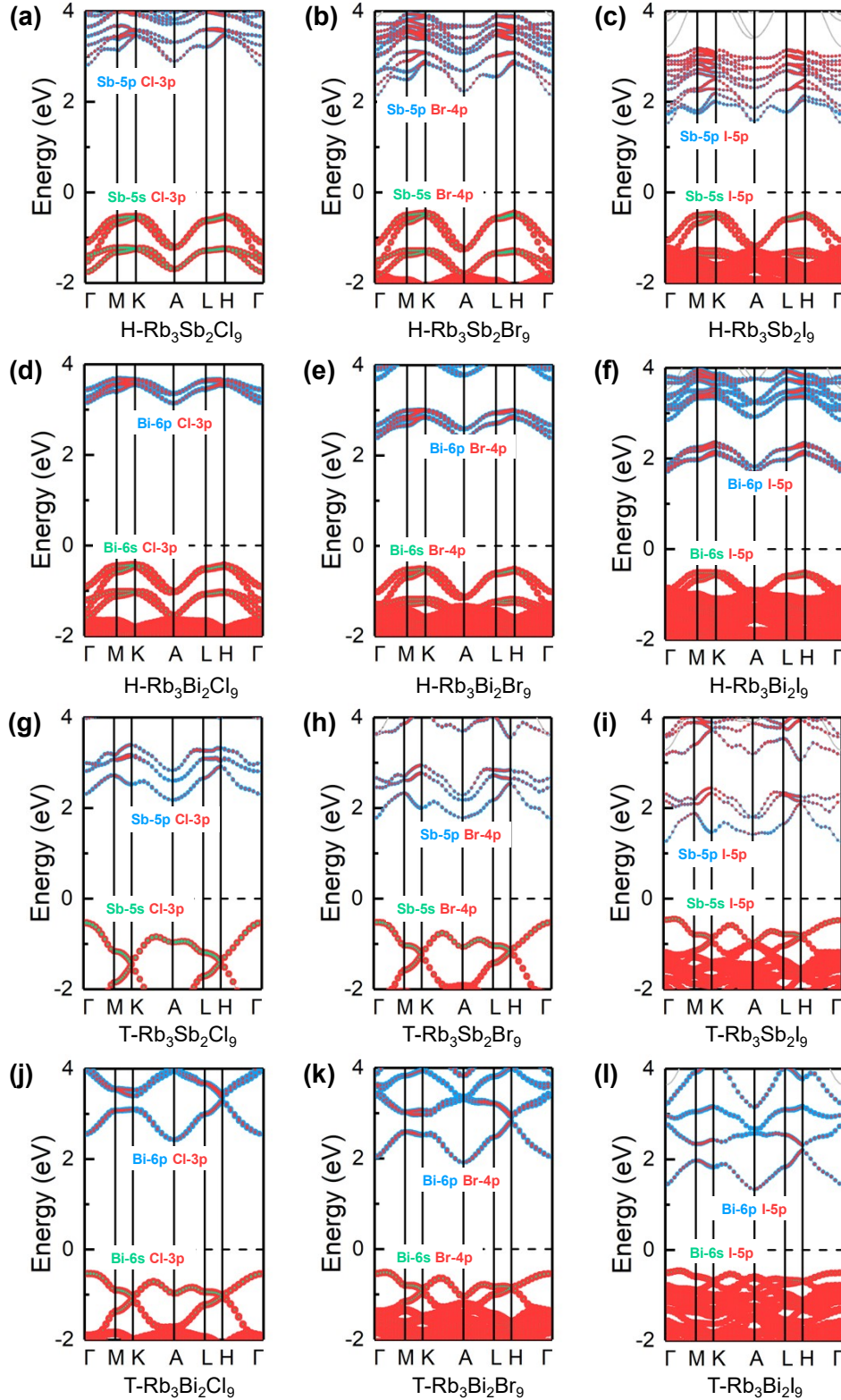


Fig. S4 Projected band structures of $\text{Rb}_3\text{B}_2\text{X}_9$ ($\text{B} = \text{Sb}, \text{Bi}$) perovskites in H and T phases. Projected band structure of (a) H-phase $\text{Rb}_3\text{Sb}_2\text{Cl}_9$, (b) H-phase $\text{Rb}_3\text{Sb}_2\text{Br}_9$, (c) H-phase $\text{Rb}_3\text{Sb}_2\text{I}_9$, (d) H-phase $\text{Rb}_3\text{Bi}_2\text{Cl}_9$, (e) H-phase $\text{Rb}_3\text{Bi}_2\text{Br}_9$, (f) H-phase $\text{Rb}_3\text{Bi}_2\text{I}_9$, (g) T-phase $\text{Rb}_3\text{Sb}_2\text{Cl}_9$, (h) T-phase $\text{Rb}_3\text{Sb}_2\text{Br}_9$, (i) T-phase $\text{Rb}_3\text{Sb}_2\text{I}_9$, (j) T-phase $\text{Rb}_3\text{Bi}_2\text{Cl}_9$, (k) T-phase $\text{Rb}_3\text{Bi}_2\text{Br}_9$, (l) T-phase $\text{Rb}_3\text{Bi}_2\text{I}_9$. The dash lines denote the position of Fermi level.

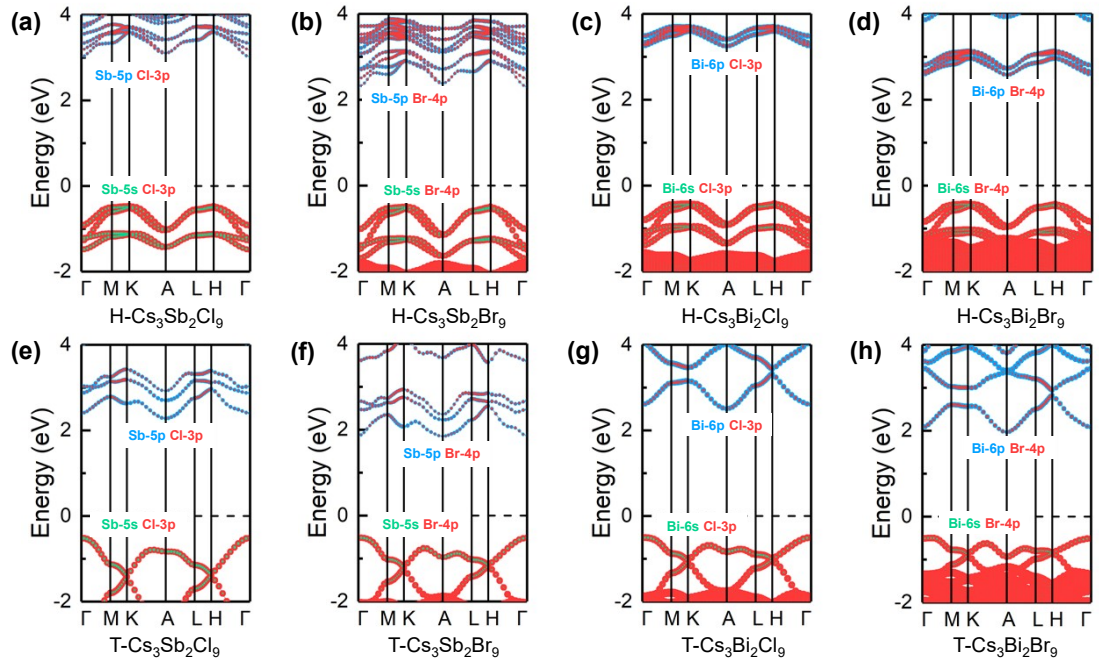


Fig. S5 Projected band structures of $\text{Cs}_3\text{B}_2\text{X}_9$ ($\text{B} = \text{Sb}, \text{Bi}$) perovskites in H and T phases. Projected band structure of (a) H-phase $\text{Cs}_3\text{Sb}_2\text{Cl}_9$, (b) H-phase $\text{Cs}_3\text{Sb}_2\text{Br}_9$, (c) H-phase $\text{Cs}_3\text{Bi}_2\text{Cl}_9$, (d) H-phase $\text{Cs}_3\text{Bi}_2\text{Br}_9$, (e) T-phase $\text{Cs}_3\text{Sb}_2\text{Cl}_9$, (f) T-phase $\text{Cs}_3\text{Sb}_2\text{Br}_9$, (g) T-phase $\text{Cs}_3\text{Bi}_2\text{Cl}_9$, (h) T-phase $\text{Cs}_3\text{Bi}_2\text{Br}_9$. The dash lines denote the position of Fermi level.

S5. Projected density of states of $\text{Cs}_3\text{Sb}_2\text{I}_9$ perovskite in H and T phases

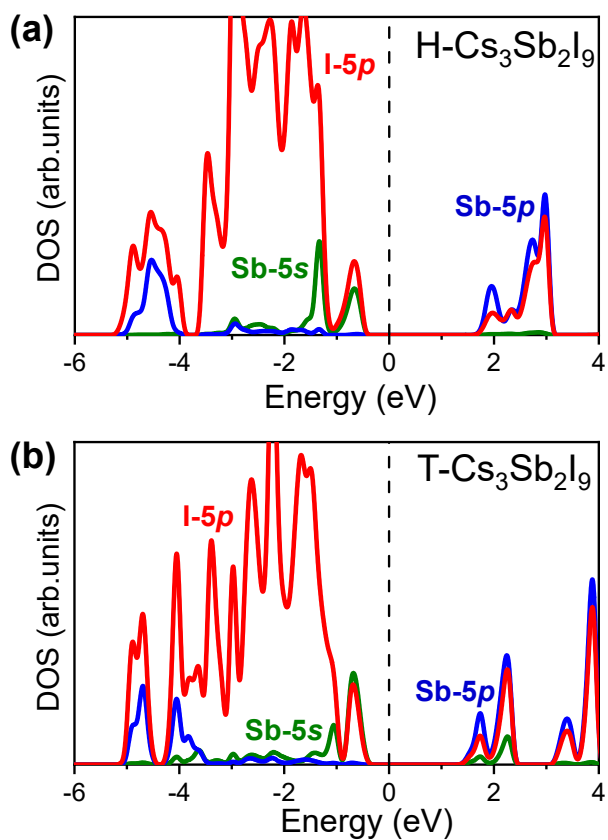


Fig. S6 Projected density of states of (a) H-phase $\text{Cs}_3\text{Sb}_2\text{I}_9$ and (b) T-phase $\text{Cs}_3\text{Sb}_2\text{I}_9$. The dashed lines denote the position of Fermi level.

S6. Illustration of the band-edge orbital coupling in $A_3B_2X_9$ perovskites

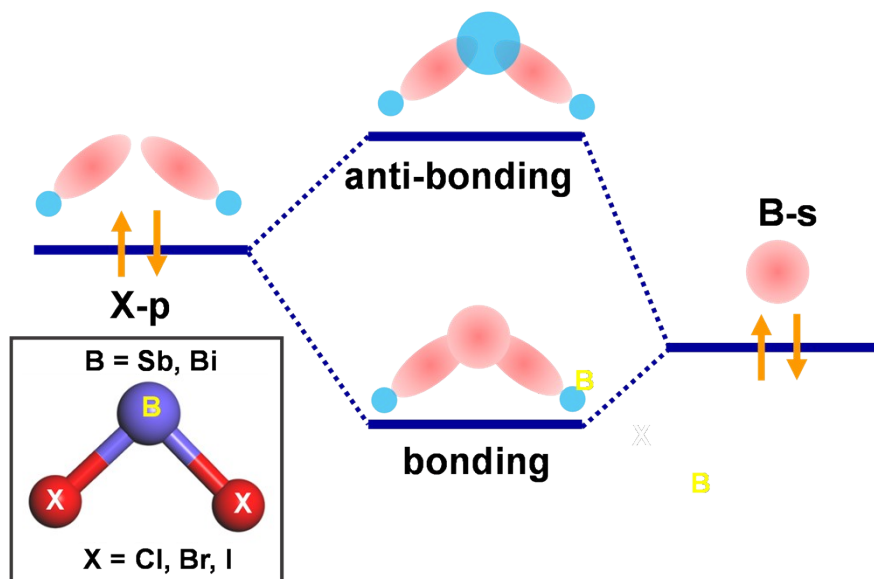


Fig. S7 Schematic illustration of the band-edge orbital interactions in $A_3B_2X_9$ perovskites with lone pairs. The $s-p$ orbital interactions between the B-site cations and X anions create filled bonding and antibonding combinations.

S7. The comparison between the calculated and experimental bandgaps of some $A_3B_2X_9$ perovskites

Table S2 The comparison of the calculated (Cal.) and experimental (Exp.) bandgaps (in eV) of bulk $A_3B_2X_9$ perovskites. The calculated bandgaps were obtained by the HSE06 functional in this work, and the experimental bandgaps were extracted from previous literatures.^{1, 4-8}

Materials	Phase structure	Cal.	Exp.
$\text{Cs}_3\text{Sb}_2\text{Cl}_9$	T	2.79	2.89 ¹
$\text{Cs}_3\text{Sb}_2\text{Br}_9$	T	2.36	2.36 ⁷
$\text{Cs}_3\text{Sb}_2\text{I}_9$	T	1.76	1.89 ⁸
$\text{Cs}_3\text{Sb}_2\text{I}_9$	H	2.21	2.02 ⁴
$\text{Cs}_3\text{Bi}_2\text{Cl}_9$	T	3.01	3.09 ⁵
$\text{Cs}_3\text{Bi}_2\text{Br}_9$	T	2.47	2.64 ⁶
$\text{Cs}_3\text{Bi}_2\text{I}_9$	H	2.29	2.06 ⁸

S8. Optical absorption spectra of $A_3B_2X_9$ perovskites in H and T phases

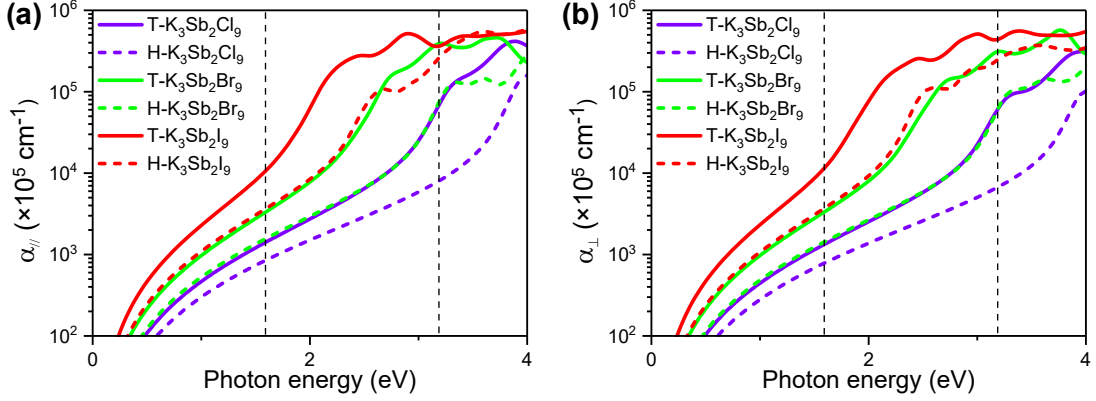


Fig. S8 Optical absorption spectra of T- and H-phase $K_3B_2X_9$ perovskites. Optical absorption spectra of T-phase and H-phase $K_3Sb_2X_9$ perovskites along (a) in-plane ($\alpha_{//}$) and (b) out-of-plane (α_{\perp}) direction. The range of dash lines corresponds to the visible-light region with the wavelength range from 390 to 780 nm.

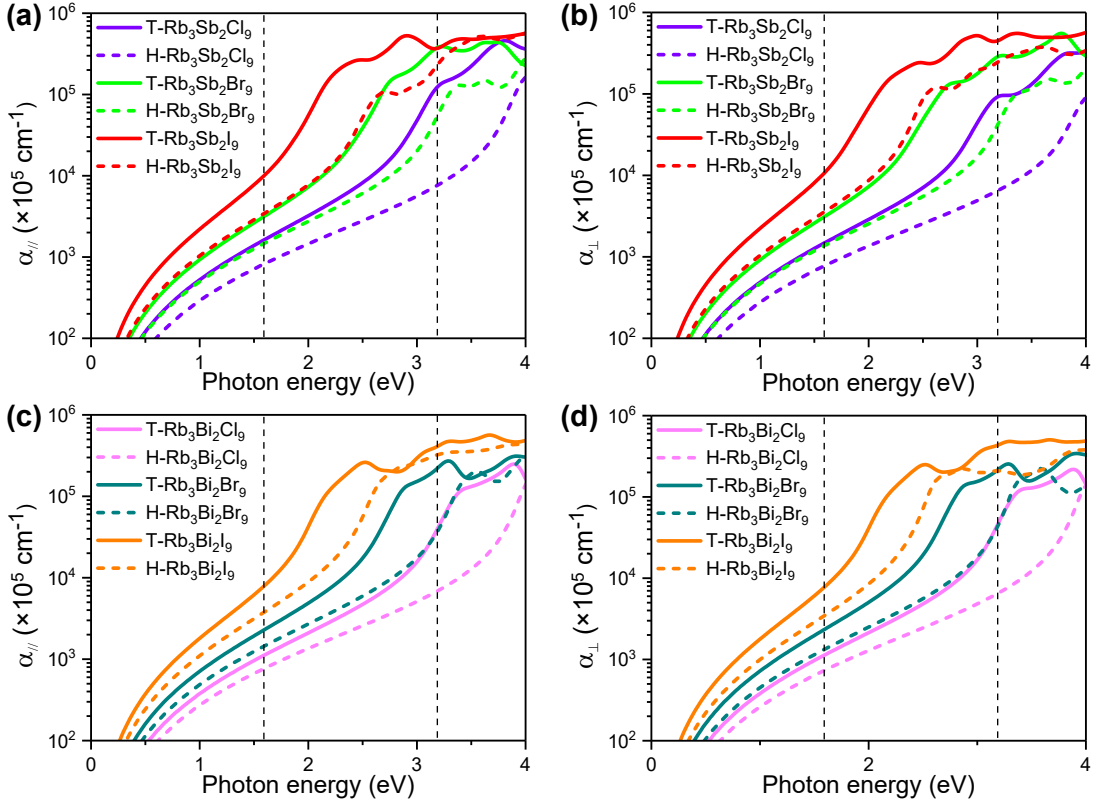


Fig. S9 Optical absorption spectra of T- and H-phase $Rb_3B_2X_9$ perovskites. Optical absorption spectra of T-phase and H-phase $Rb_3Sb_2X_9$ perovskites along (a) in-plane ($\alpha_{//}$) and (b) out-of-plane (α_{\perp}) direction. Optical absorption spectra of T-phase and H-phase $Rb_3Bi_2X_9$ perovskites along (c) in-plane ($\alpha_{//}$) and (d) out-of-plane (α_{\perp}) direction. The range of dash lines corresponds to the visible-light region with the wavelength range from 390 to 780 nm.

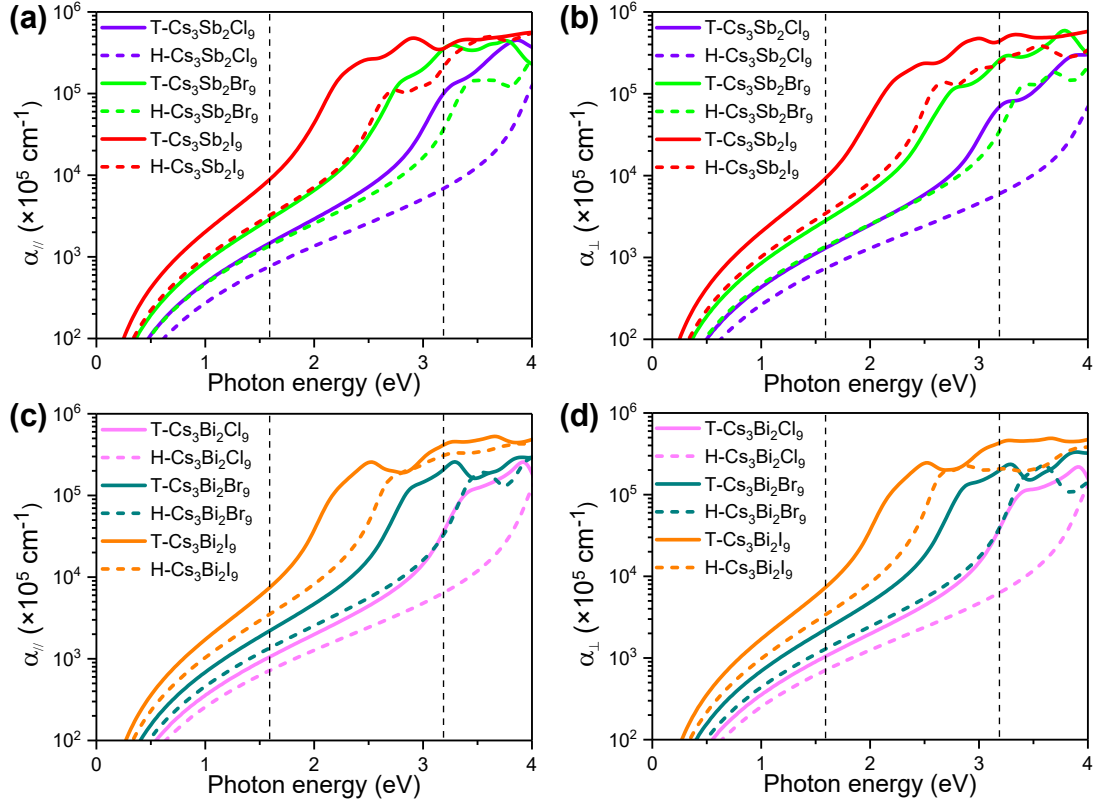


Fig. S10 Optical absorption spectra of T- and H-phase $\text{Cs}_3\text{B}_2\text{X}_9$ perovskites. Optical absorption spectra of T-phase and H-phase $\text{Cs}_3\text{Sb}_2\text{X}_9$ perovskites along (a) in-plane ($\alpha_{//}$) and (b) out-of-plane (α_{\perp}) direction. Optical absorption spectra of T-phase and H-phase $\text{Cs}_3\text{Bi}_2\text{X}_9$ perovskites along (c) in-plane ($\alpha_{//}$) and (d) out-of-plane (α_{\perp}) direction. The range of dash lines corresponds to the visible-light region with the wavelength range from 390 to 780 nm.

S9. The computational details for intrinsic defects of T-phase Cs₃Sb₂I₉

In order to understand the defect formation in A₃B₂X₉ perovskites, we used T-phase Cs₃Sb₂I₉ as an example. Ten potential intrinsic point defects were considered, including three vacancy defects (V_{Cs}, V_{Sb}, and V_I), four antisite defects (Sb_{Cs}, Cs_{Sb}, Cs_I, Sb_I), and three interstitial atoms (I_{Cs}, I_{Sb}, and I_I). The defect models were constructed by introducing the point defects into a (2×2×2) supercell including 112 atoms. The stability of these intrinsic point defects was evaluated by the defect formation energy (ΔH_f) as follows,⁹

$$\Delta H_f = E_D - E_P + \sum_i \Delta n_i \mu_i \quad (1)$$

where E_D is the total energy of the defective system, E_P is the total energy of the perfect Cs₃Sb₂I₉ system, μ_i is the chemical potential of atomic species i ($i = \text{Cs, Sb, and I}$), and Δn_i is the difference of the number of atomic species i between the defective and perfect systems. In the equilibrium conditions, the chemical potential of Cs, Sb, and I should satisfy $3\mu_{\text{Cs}} + 2\mu_{\text{Sb}} + 9\mu_{\text{I}} = E_T(\text{Cs}_3\text{Sb}_2\text{I}_9)$, where E_T is the total energy of Cs₃Sb₂I₉ per formula cell. It can be transformed into the following equation,

$$3\Delta\mu_{\text{Cs}} + 2\Delta\mu_{\text{Sb}} + 9\Delta\mu_{\text{I}} = \Delta H_f(\text{Cs}_3\text{Sb}_2\text{I}_9) \quad (2)$$

where $\Delta H_f(\text{Cs}_3\text{Sb}_2\text{I}_9)$ is the enthalpy of formation of Cs₃Sb₂I₉. In order to ensure the formation of Cs₃Sb₂I₉, the secondary phases CsI and SbI₃ as well as the element crystals Cs, Sb, and I need to be avoided, so the chemical potentials and enthalpies of binary compounds should satisfy the following constraint conditions:

$$\Delta\mu_{\text{Cs}} + \Delta\mu_{\text{I}} < \Delta H_f(\text{CsI}) \quad (3)$$

$$\Delta\mu_{\text{Sb}} + 3\Delta\mu_{\text{I}} < \Delta H_f(\text{SbI}_3) \quad (4)$$

By means of the equations (2)–(4), the allowed range of chemical potentials for the formation of T-phase Cs₃Sb₂I₉ can be determined, as shown in the gray shaded region of Fig. S11. The allowed chemical potential range is surrounded by the critical points A–C. The point A corresponds to I-rich condition, and the chemical potential at the points B and C can be determined by the equation (2). According to the allowed

chemical potential range, we calculated the defect formation energy of ten intrinsic point defects, as listed in Table S3. It can be seen that the Cs vacancy (V_{Cs}) and I vacancy (V_I) are the most two stable defect structures in the allowed chemical potential range. Furthermore, we calculated the band structure of $Cs_3Sb_2I_9$ with V_{Cs} and V_I , respectively. The band structure of perfect $Cs_3Sb_2I_9$ was also calculated for comparison. As shown in Fig. S12, $Cs_3Sb_2I_9$ with V_{Cs} indicates a p-type character and $Cs_3Sb_2I_9$ with V_I exhibits a n-type character. For both of two defect structures, they do not induce the formation of deep defect levels.

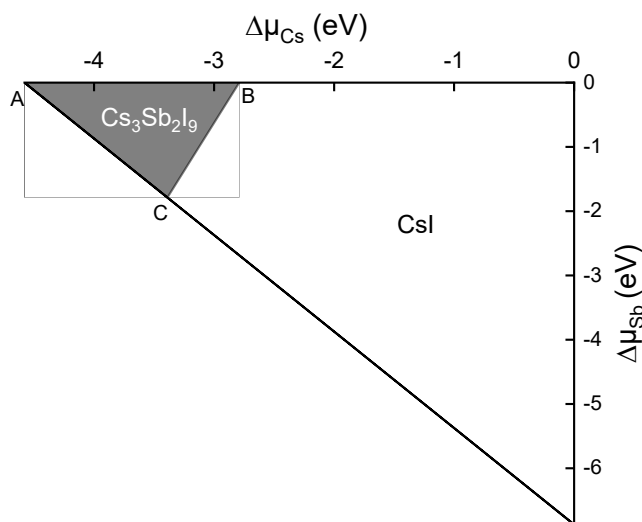


Fig. S11 Calculated stable phase diagram of T-phase $Cs_3Sb_2I_9$ as a function of the chemical potentials of Cs (μ_{Cs}) and Sb (μ_{Sb}). The gray area is the thermodynamically stable range for the equilibrium growth of $Cs_3Sb_2I_9$. The stable region is surrounded by points A-C.

Table S3 Defect formation energies (ΔH_f) of ten intrinsic point defects in T-phase $Cs_3Sb_2I_9$ under the equilibrium conditions of three chemical potential conditions. The three chemical potential conditions correspond to three critical points A, B, and C in Fig. S11.

Intrinsic defects	Defect formation energy ΔH_f (in eV)		
	A	B	C
V_{Cs}	-0.24	1.55	0.95
V_{Sb}	3.22	3.22	1.43
V_I	1.93	1.33	1.93
Sb_{Cs}	1.81	3.60	4.79
Cs_{Sb}	4.98	3.19	2.00
Cs_I	4.51	2.12	3.32
Sb_I	2.75	2.15	4.54
I_{Cs}	3.76	1.97	2.57
I_{Sb}	1.77	1.77	3.56
I_I	1.35	1.95	1.35

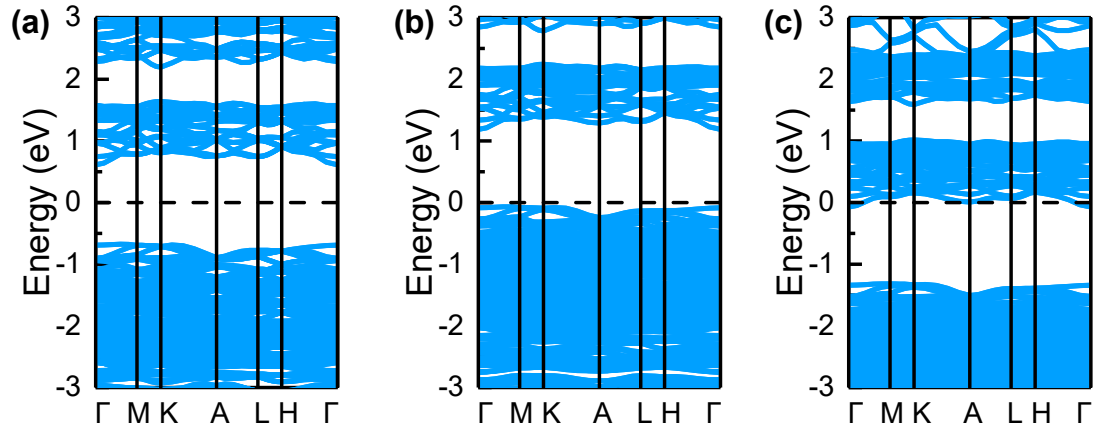


Fig. S12 Band structure of (a) perfect T-phase $\text{Cs}_3\text{Sb}_2\text{I}_9$, (b) T-phase $\text{Cs}_3\text{Sb}_2\text{I}_9$ with a Cs vacancy, (c) T-phase $\text{Cs}_3\text{Sb}_2\text{I}_9$ with a I vacancy. The dash lines denote the position of Fermi level.

S10. Thickness effect on electronic structures of 2D T-phase $\text{Cs}_3\text{B}_2\text{X}_9$ nanosheets

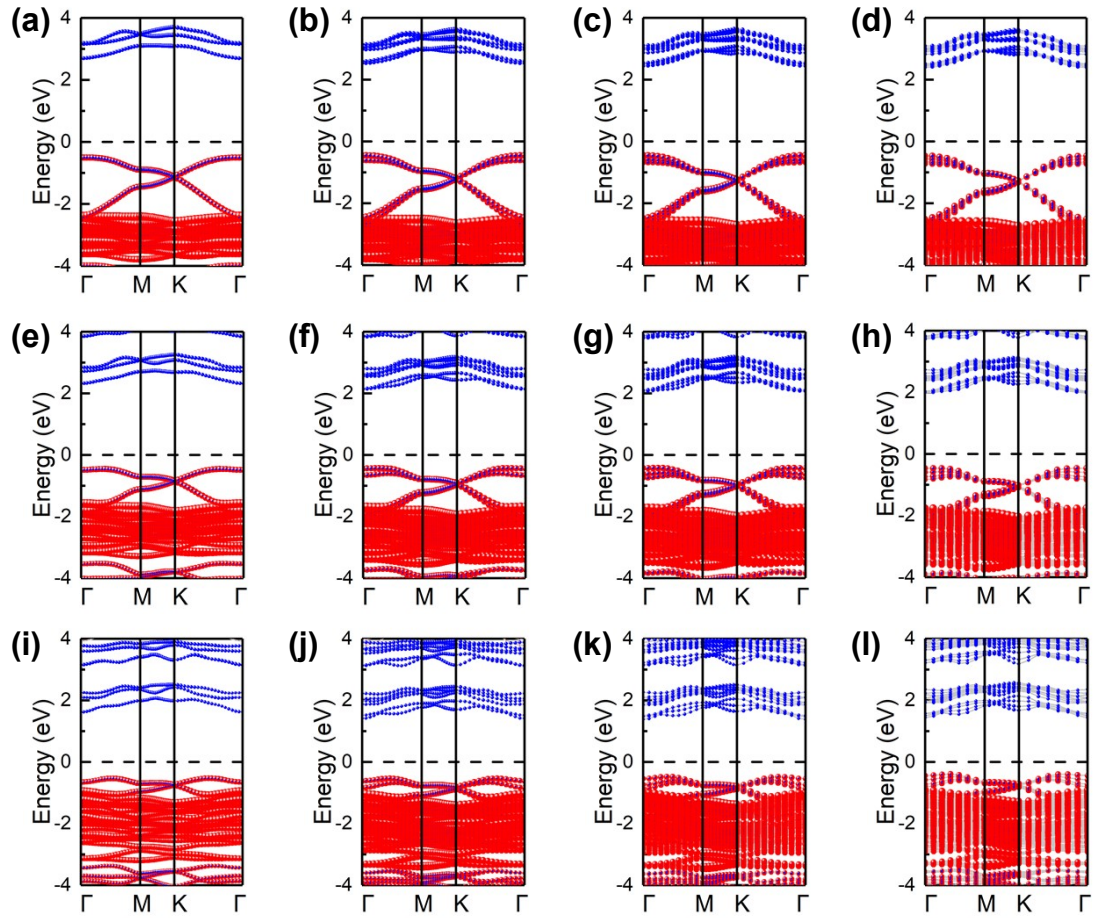


Fig. S13 Thickness effect on band structures of 2D T-phase $\text{Cs}_3\text{Sb}_2\text{X}_9$ ($\text{X} = \text{Cl}, \text{Br}, \text{I}$) nanosheets. Projected band structure of (a-d) $\text{Cs}_3\text{Sb}_2\text{Cl}_9$, (e-h) $\text{Cs}_3\text{Sb}_2\text{Br}_9$, (i-l) $\text{Cs}_3\text{Sb}_2\text{I}_9$ with the thickness range from the monolayer (1L) to tetralayer (4L). The blue and red bands are contributed by Sb and X, respectively. The dash lines denote the position of Fermi level.

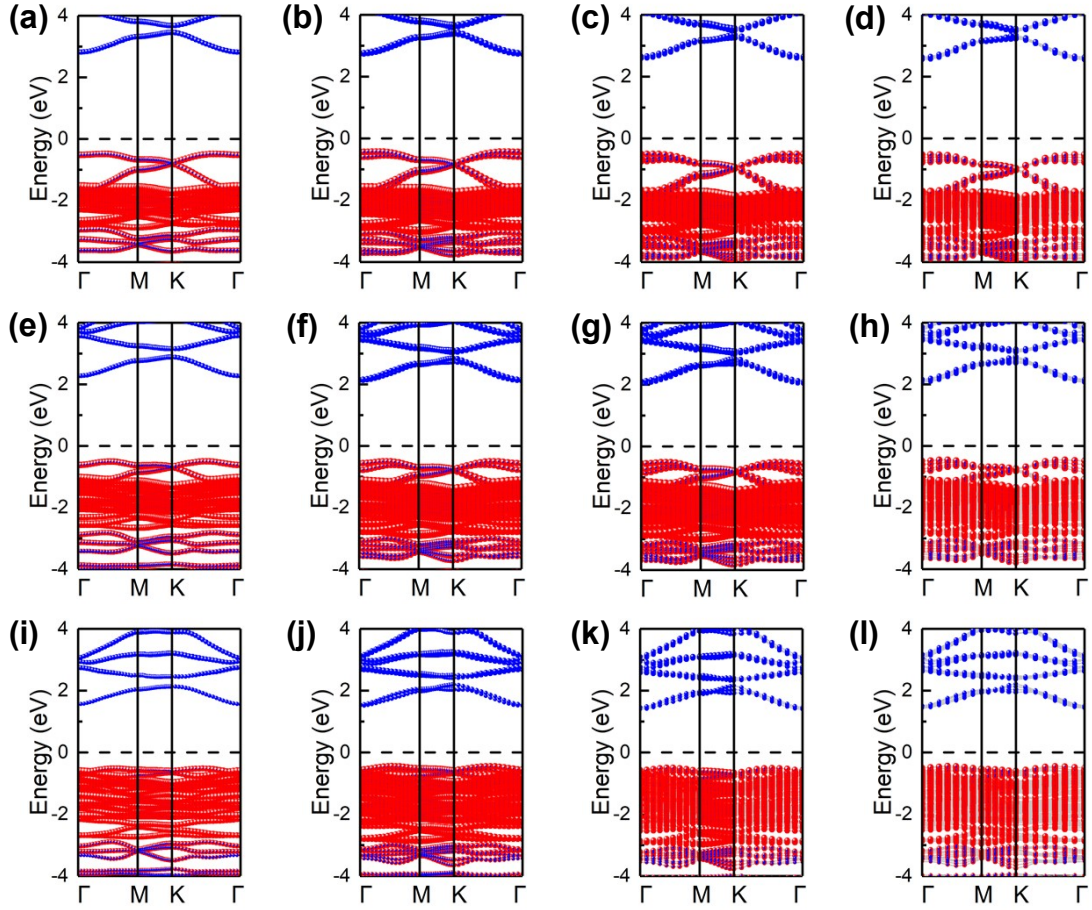


Fig. S14 Thickness effect on band structures of 2D T-phase $\text{Cs}_3\text{Bi}_2\text{X}_9$ ($\text{X} = \text{Cl}, \text{Br}, \text{I}$) nanosheets. Projected band structure of (a-d) $\text{Cs}_3\text{Bi}_2\text{Cl}_9$, (e-h) $\text{Cs}_3\text{Bi}_2\text{Br}_9$, (i-l) $\text{Cs}_3\text{Bi}_2\text{I}_9$ with the thickness range from the monolayer (1L) to tetralayer (4L). The blue and red bands are contributed by Bi and X, respectively. The dash lines denote the position of Fermi level.

S11. Thickness effect on optical absorption of 2D T-phase $\text{Cs}_3\text{B}_2\text{X}_9$ nanosheets

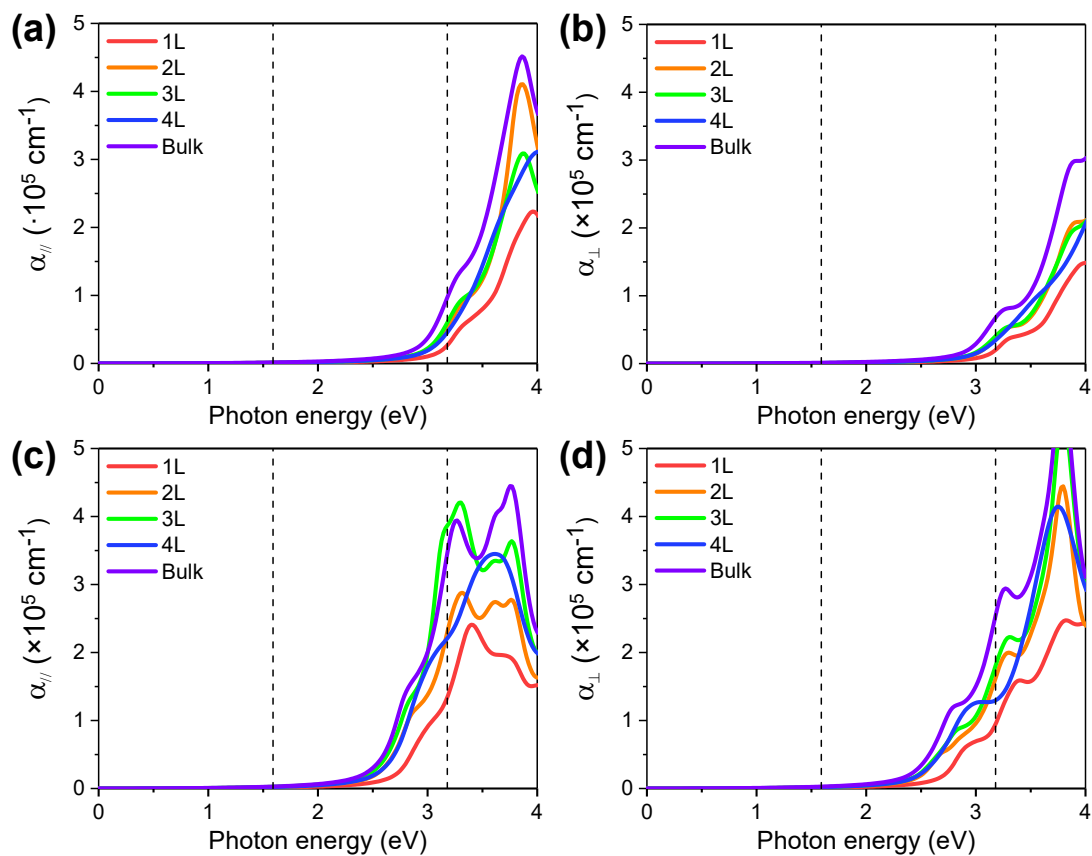


Fig. S15 Thickness effect on optical absorption spectra of 2D T-phase $\text{Cs}_3\text{Sb}_2\text{X}_9$ (X = Cl, Br) nanosheets. (a,b) Optical absorption spectra of 2D T-phase $\text{Cs}_3\text{Sb}_2\text{Cl}_9$ nanosheets with the thickness range from 1L to 4L along the (a) in-plane ($\alpha_{//}$) and (b) out-of-plane (α_{\perp}) polarization direction. (c,d) Optical absorption spectra of 2D T-phase $\text{Cs}_3\text{Sb}_2\text{Br}_9$ nanosheets with the thickness range from 1L to 4L along the (c) in-plane ($\alpha_{//}$) and (d) out-of-plane (α_{\perp}) polarization direction. The range of dash lines corresponds to the visible region with the range of wavelength from 390 to 780 nm.

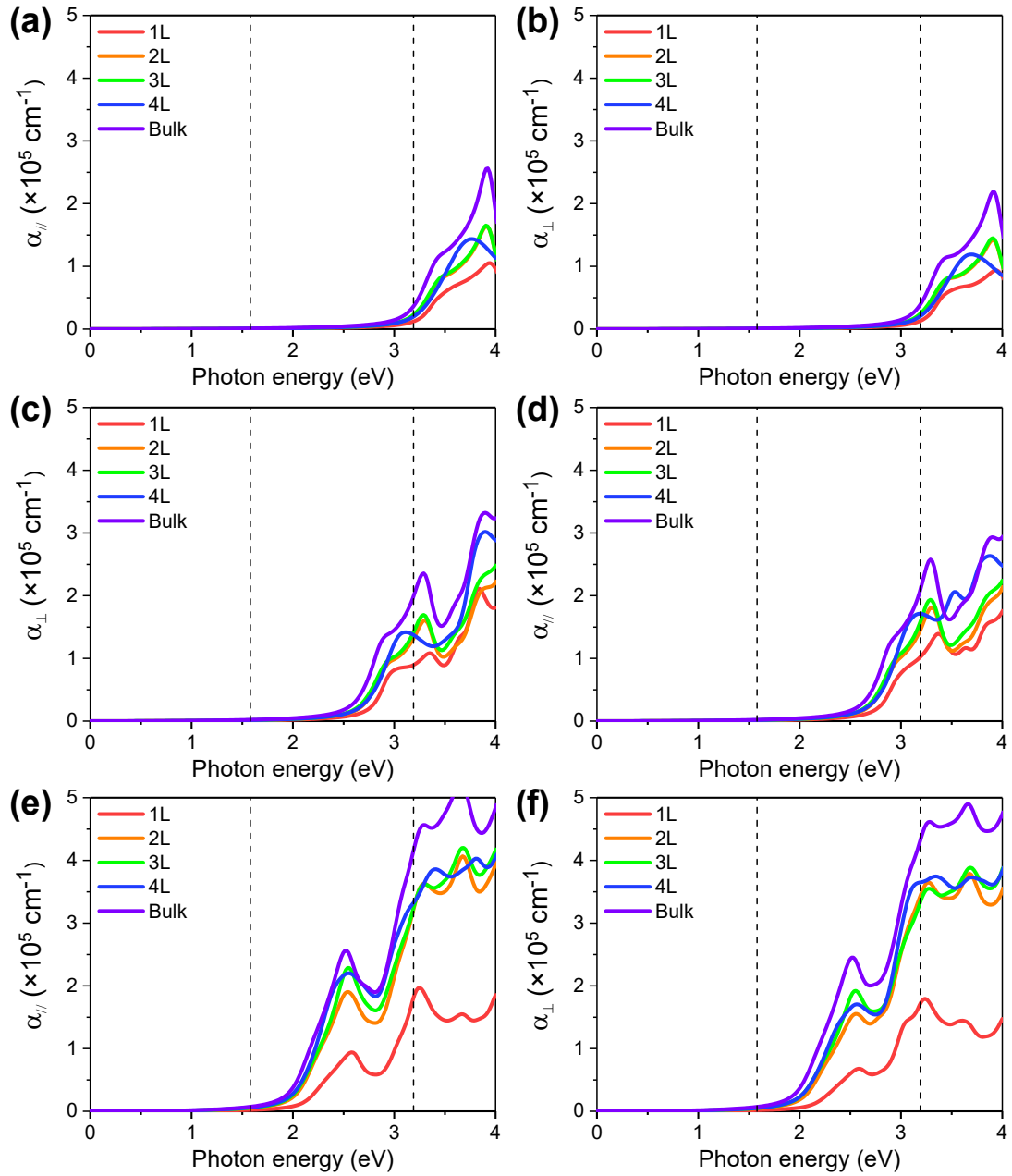


Fig. S16 Thickness effect on optical absorption spectra of 2D T-phase $\text{Cs}_3\text{Bi}_2\text{X}_9$ ($X = \text{Cl}, \text{Br}, \text{I}$) nanosheets. (a,b) Optical absorption spectra of 2D T-phase $\text{Cs}_3\text{Bi}_2\text{Cl}_9$ nanosheets with the thickness range from 1L to 4L along the (a) in-plane ($\alpha_{//}$) and (b) out-of-plane (α_{\perp}) polarization direction. (c,d) Optical absorption spectra of 2D T-phase $\text{Cs}_3\text{Bi}_2\text{Br}_9$ nanosheets with the thickness range from 1L to 4L along the (c) in-plane ($\alpha_{//}$) and (d) out-of-plane (α_{\perp}) polarization direction. (e,f) Optical absorption spectra of 2D T-phase $\text{Cs}_3\text{Bi}_2\text{I}_9$ nanosheets with the thickness range from 1L to 4L along the (e) in-plane ($\alpha_{//}$) and (f) out-of-plane (α_{\perp}) polarization direction. The range of dash lines corresponds to the visible region with the range of wavelength from 390 to 780 nm.

References

- 1 A. Pradhan, S. C. Sahoo, A. K. Sahu and S. L. Samal, *Cryst. Growth Des.*, 2020, **20**, 3386-3395.
- 2 J. Mao, Z. Zheng, Z. Xiong, P. Huang, G. Ding, R. Wang, Z. Wang, J. Yang, Y. Zhou, T. Zhai and S. Han, *Nano Energy*, 2020, **71**, 104616.
- 3 K. M. McCall, Z. Liu, G. Trimarchi, C. C. Stoumpos, W. Lin, Y. He, I. Hadar, M. G. Kanatzidis and B. W. Wessels, *ACS Photonics* 2018, **5**, 3748-3762.
- 4 J. Mei, M. Liu, P. Vivo and V. Pecunia, *Adv. Funct. Mater.*, 2021, **31**, 2106295.
- 5 T. Geng, Y. Shi, Z. Liu, D. Zhao, Z. Ma, K. Wang, Q. Dong, G. Xiao and B. Zou, *J. Phys. Chem. Lett.*, 2022, **13**, 11837-11843.
- 6 J. Jin, L. N. Quan, M. Gao, C. Chen, P. Guo and P. Yang, *J. Phys. Chem. C*, 2023, **127**, 3523-3531.
- 7 J. Zhang, Y. Yang, H. Deng, U. Farooq, X. Yang, J. Khan, J. Tang and H. Song, *ACS Nano*, 2017, **11**, 9294-9302.
- 8 K. M. McCall, C. C. Stoumpos, S. S. Kostina, M. G. Kanatzidis and B. W. Wessels, *Chem. Mater.*, 2017, **29**, 4129-4145.
- 9 S. H. Wei and S. B. Zhang, *Phys. Rev. B*, 2002, **66**, 155211.